Supplementary Information for

Mn-inlaid antiphase boundaries in perovskite structure

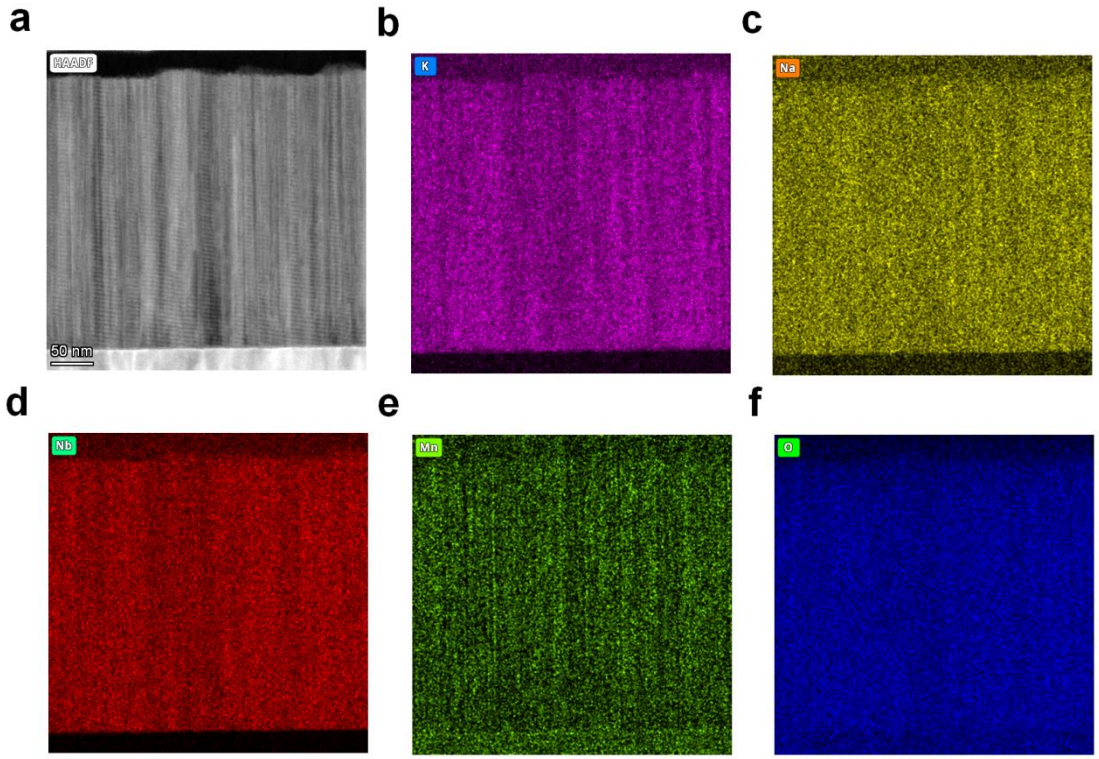

Supplementary Fig. 1| The cross-sectional microstructure and element mappings of a KNN-M thin film grown on LSSO buffered STO substrates. a, High angle annular dark field scanning transmission electron microscopy (HAADF-STEM) image in the out-of-plane direction. **b-f**, Element mappings of K, Na, Nb, Mn, and O in the KNN-M thin films, respectively.

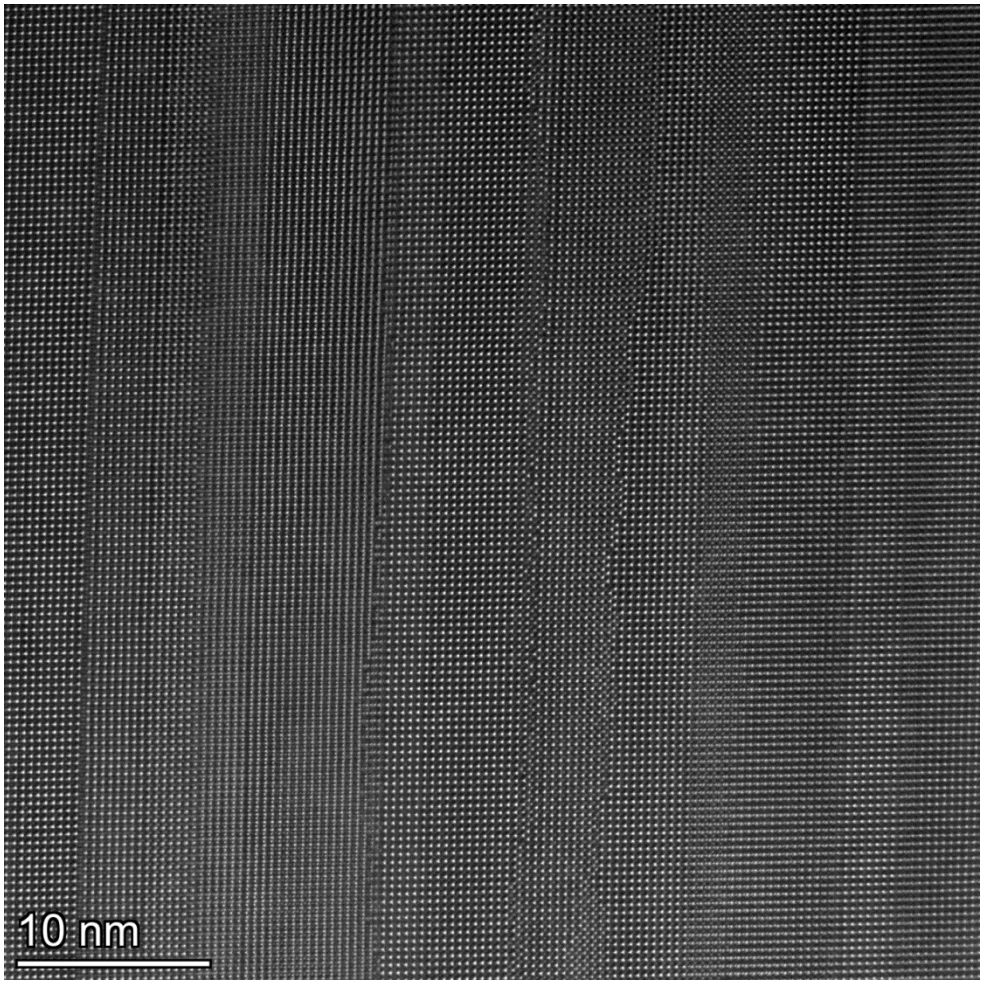

Supplementary Fig. 2| Cross-sectional HAADF image of KNN-M thin films.

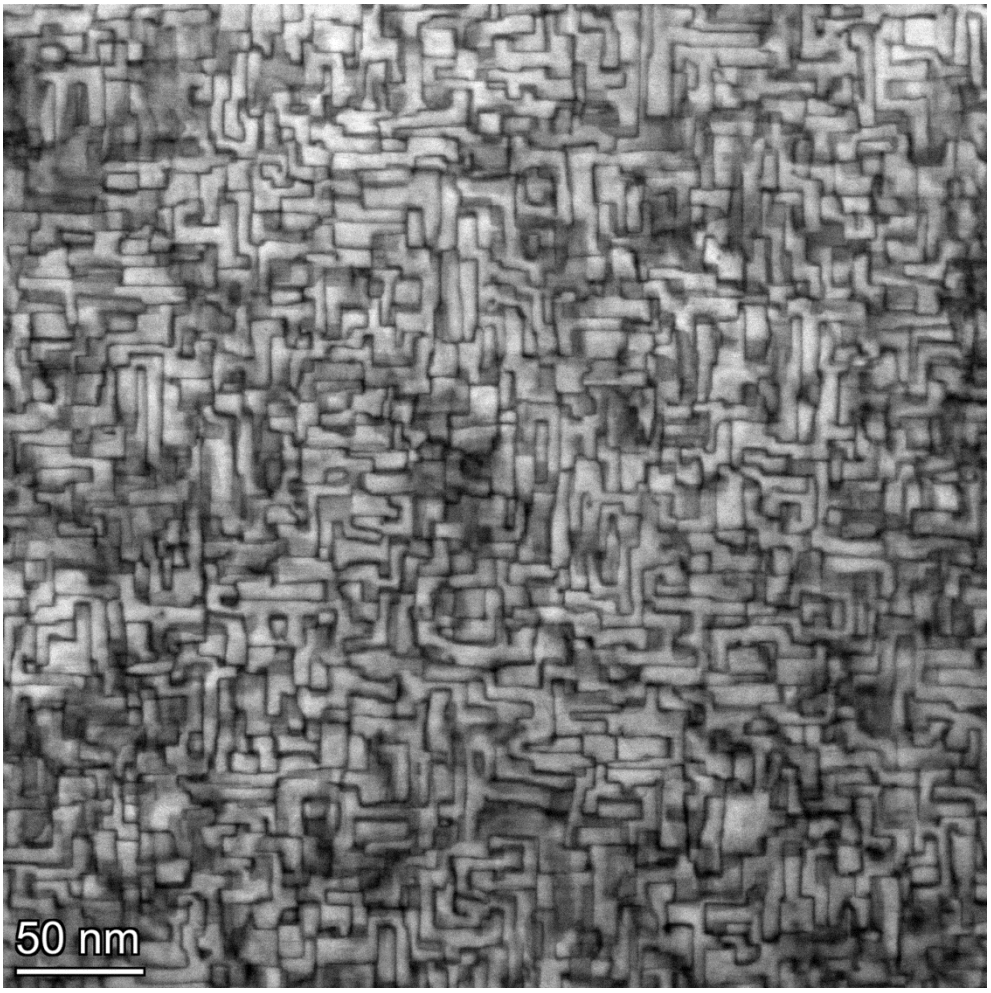

Supplementary Fig. 3| In-plane ABF image of KNN-M thin films.

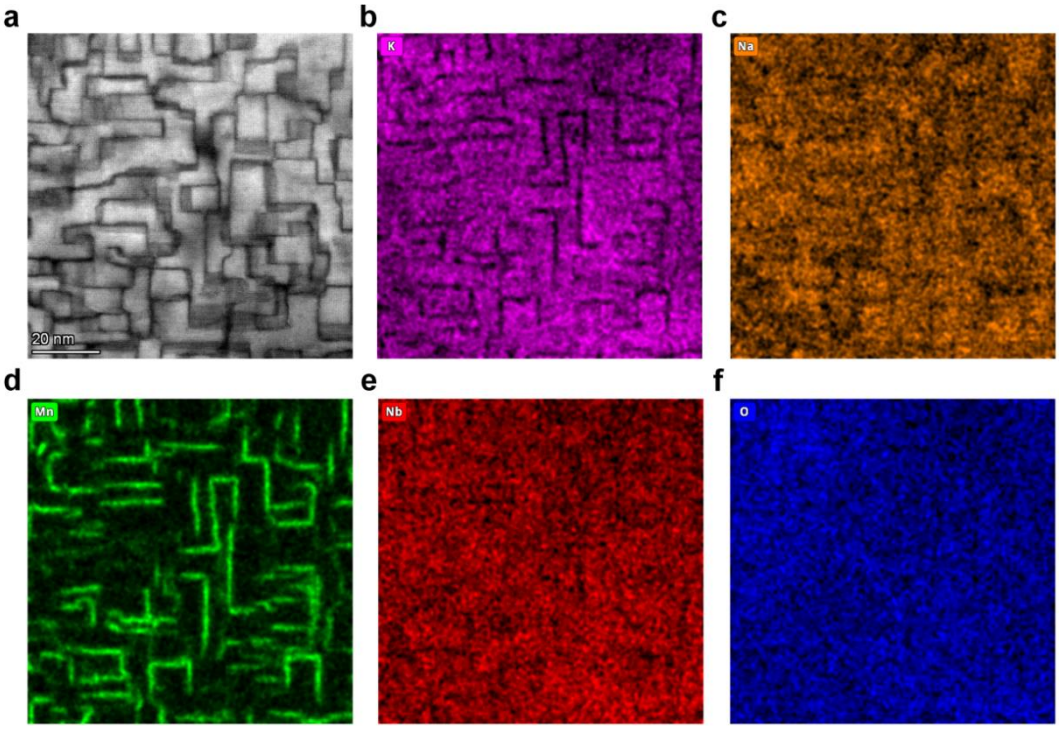

Supplementary Fig. 4| The microstructure and chemical composition of KNN-M thin films along in-plane direction. a, ADF image of KNN-M thin films. **b-f,** element mappings of K, Na, Mn, Nb, and O in KNN-M thin films, respectively.

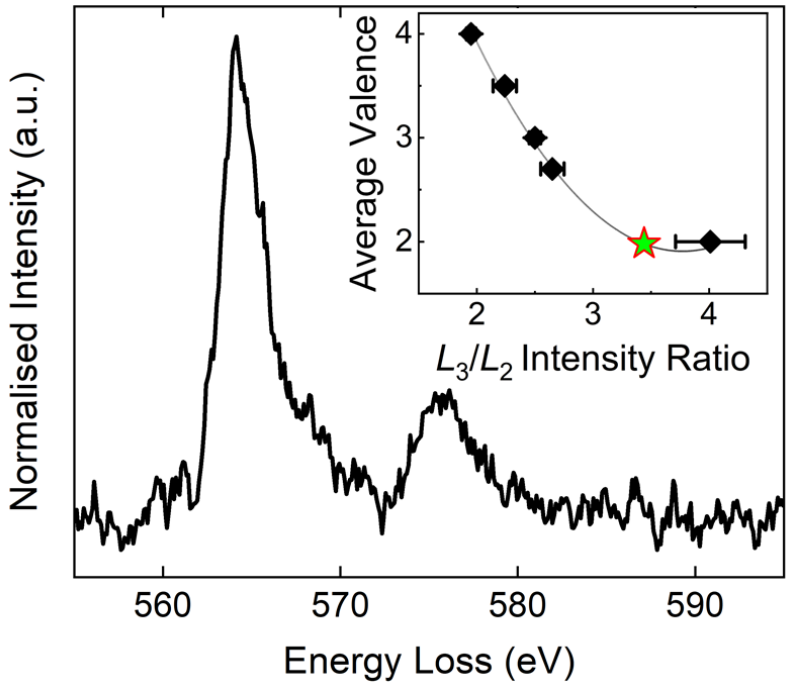

Supplementary Fig. 5| EELS of L_3/L_2 white-line of Mn elements for the KNN-M thin films. The insert shows the calibration curve used to quantify the average Mn valence in unknown samples (*34, 35*), where the manganese mainly show Mn^{2+} characteristics as indicated by the icon of star. Plural-scattering correction was applied prior to the calculation of L_3/L_2 intensity ratios and error bars represent one standard deviation about the mean.

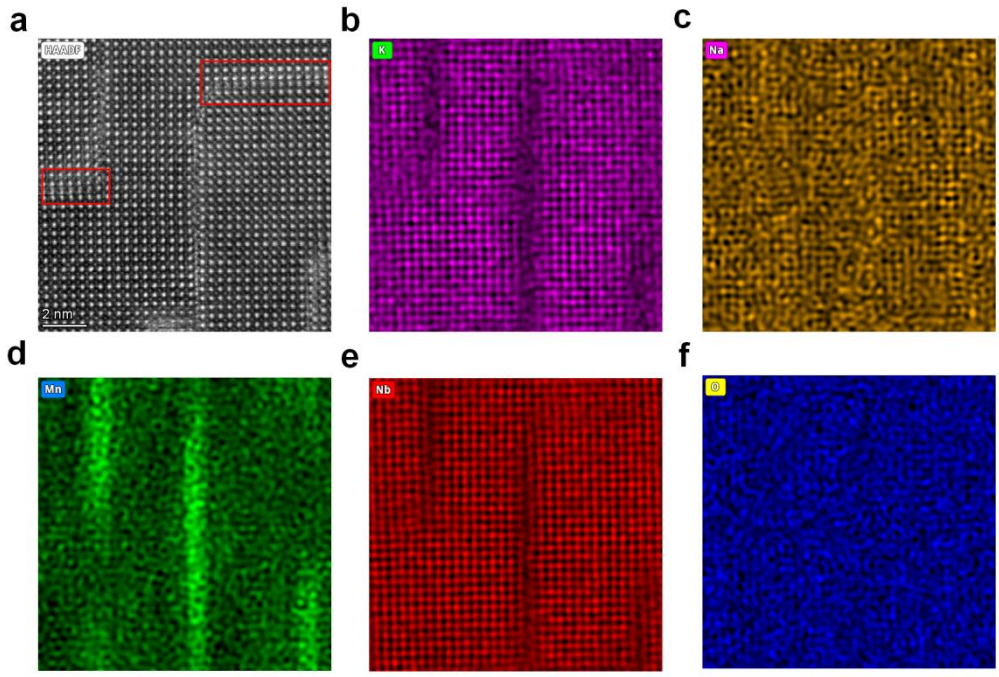

Supplementary Fig. 6| The microstructure and element mappings of KNN-M thin films along in-plane direction. a, ADF image of KNN-M thin films. b-f, Elements composition distribution of K, Na, Mn, Nb, and O in KNN-M thin films, respectively.

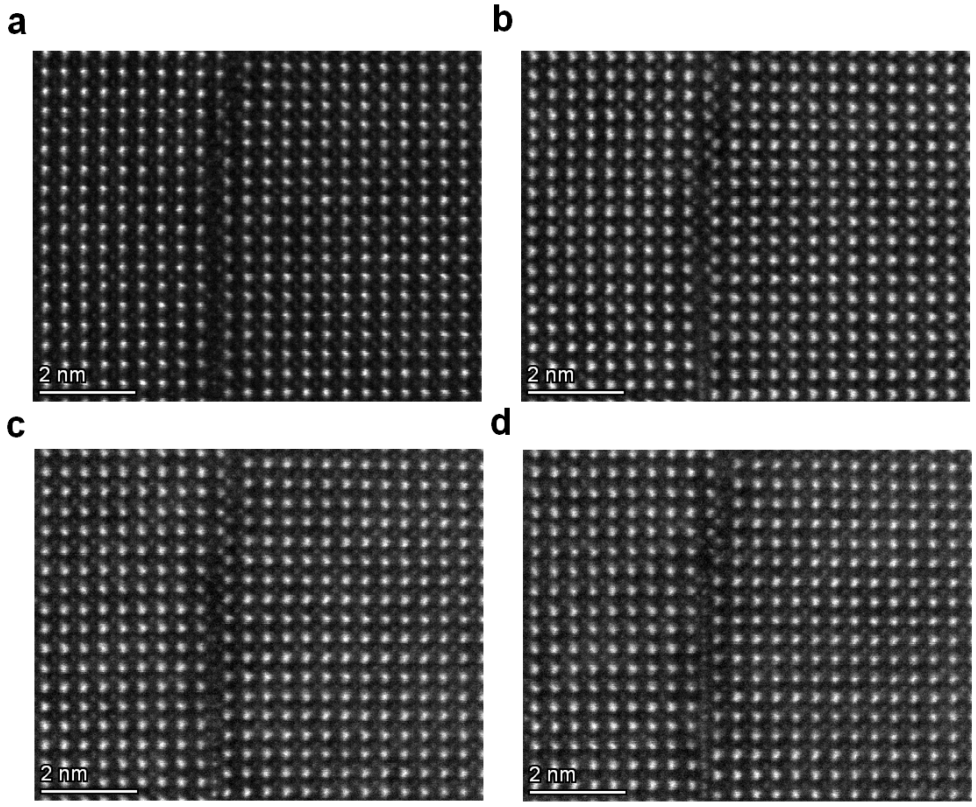

Supplementary Fig. 7| Microstructure evolution of I-type Mn-inlaid antiphase boundaries with electron beam irradiations. a-d The HAADF image of I-type Mn-inlaid antiphase boundaries with different irradiation time. From **a** to **d**, two

atomic layers can transfer to single atomic layer at the boundary.

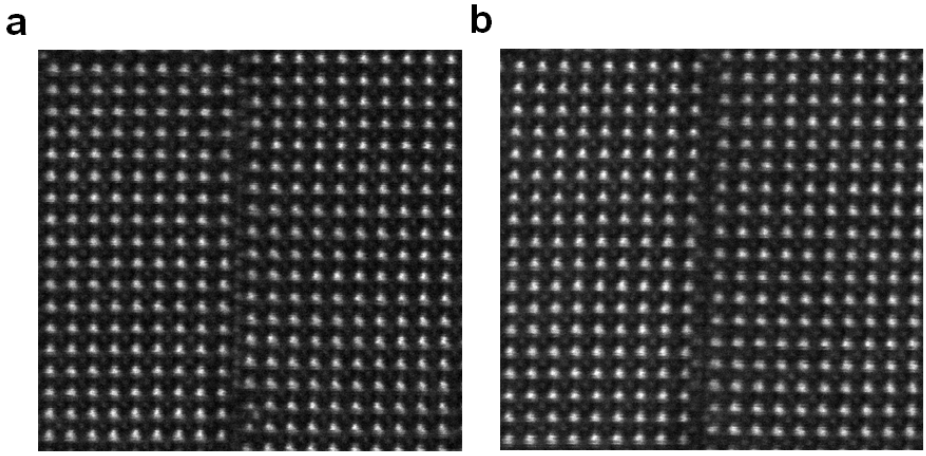

Supplementary Fig. 8| Microstructure evolution of I-type Mn-layered antiphase boundaries with electron beam irradiations. a-b The HAADF image of I-type Mn-inlaid antiphase boundaries with different irradiation time. From **a** to **b**, single layer can transfer to two atomic layers at the boundaries.

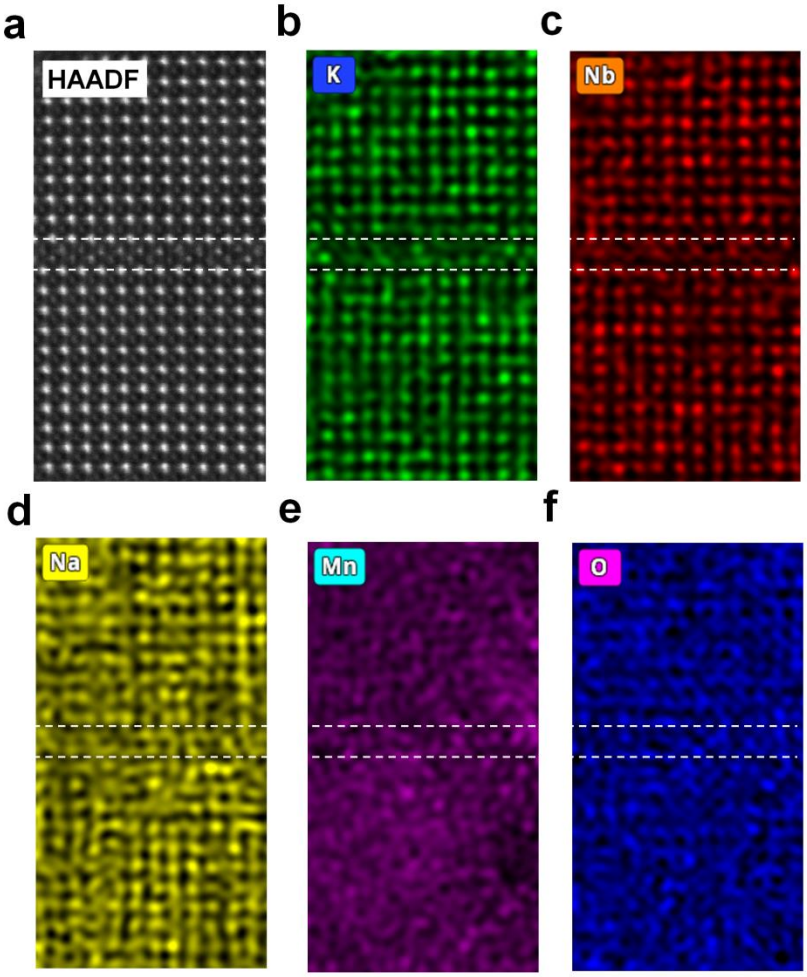

Supplementary Fig. 9| The microstructure and chemical composition of II-type antiphase boundaries along the in-plane direction. a, ADF image II-type antiphase

boundaries in KNN-M thin films. **b-f**, Corresponding element mappings of K, Nb, Na, Mn, and O.

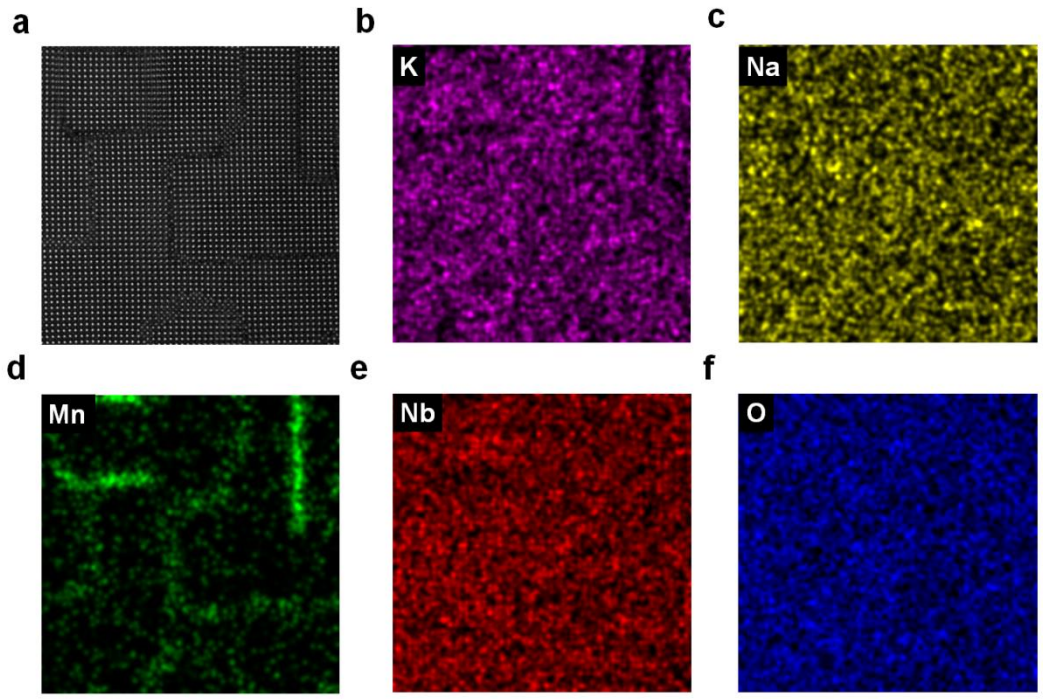

Supplementary Fig. 10| The microstructure and chemical composition mapping of KNN-M thin films along in-plane direction. a, In-plane ADF image of KNN-M thin films. **b-f**, corresponding elements composition distribution of K, Nb, Na, Mn, and O, respectively. Here, Mn enrichments can be seen for both antiphase boundaries, where the I-type antiphase boundaries show higher content Mn enrichment but the II-type antiphase boundaries show relatively low content Mn.

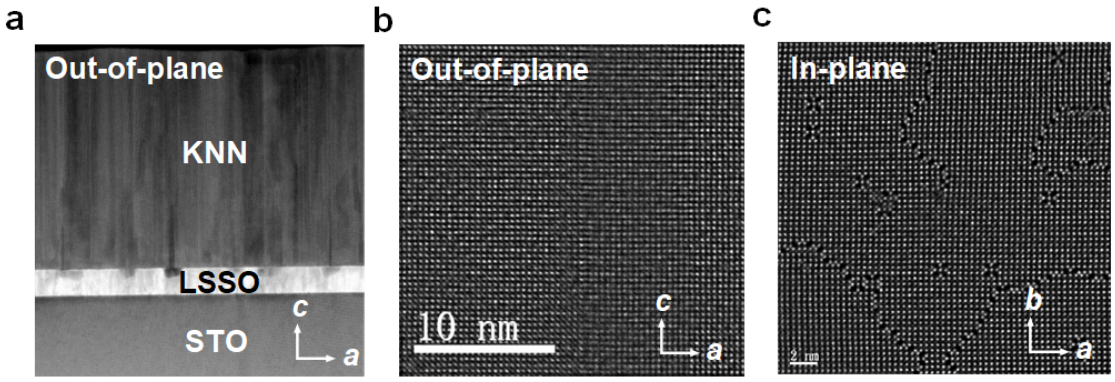

Supplementary Fig. 11| The cross-sectional morphology for a pure KNN film grown onto the LSSO buffered STO substrate obtained with TEM, showing a nanocolumnar structure. a, HAADF image of KNN-M thin films. **b**, atomic resolution HAADF image of KNN-M thin films in the out-of-plane direction, **c**, atomic resolution HAADF image of KNN-M thin films in the in-plane direction.

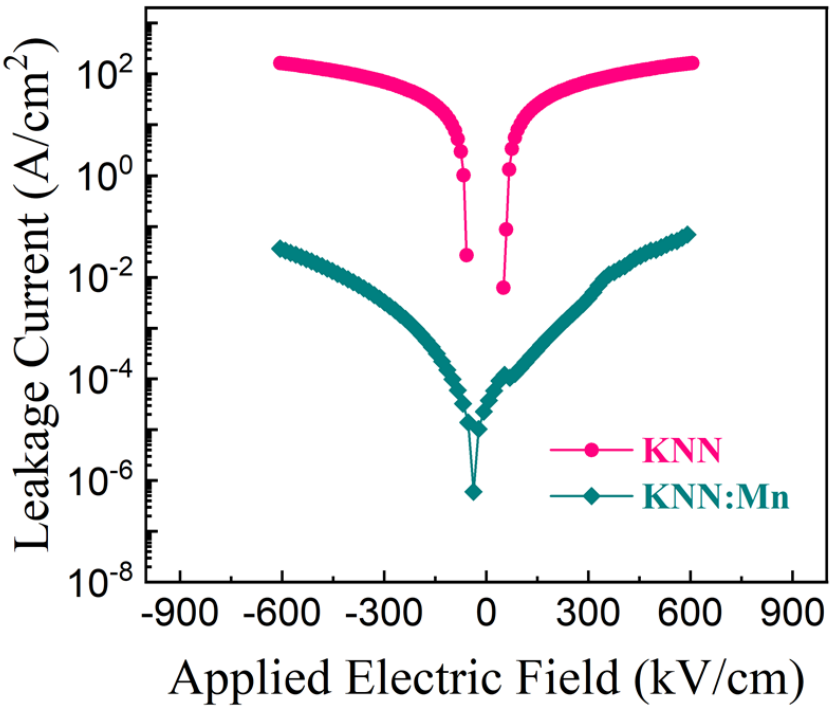

Supplementary Fig. 12| The leakage current curve plotted against applied electric field (*I-E* curve) for intrinsic KNN and KNN-M thin films, where the pure KNN thin films show high leakage current even at low applied fields due to the K/Na deficiency during deposition at higher temperatures.

Supplementary Note 1| Charge equilibrium at Mn-inlaid antiphase boundaries

Supplementary Fig.13 illustrates the schematic diagram of charge balance for I-type antiphase boundaries. In this configuration, the perovskite lattice undergoes a shift of 1/2 unit cell along both in-plane and out-of-plane directions (Supplementary Fig. 13a), resulting in the formation of an additional O vacancy and an A-site vacancy at the antiphase boundary for each unit cell (Supplementary Fig. 13b). By occupying the O and A-site vacancies with an anion O^{2-} and a cation Mn^{2+}, respectively, the charges can be equilibrium (Supplementary Fig.

13c). Additionally, considering the significant volatilization of K/Na at the boundaries, the antiphase boundaries are predominantly composed of Mn and O atoms as observed experimentally.

In Type-I antiphase boundaries, the atomic site occupations occur at both the A-site and O-site in the perovskite structure. Therefore, theoretically, both Mn and O atoms can randomly occupy the atomic site at the boundaries. In experiments, we can adjust the deposition process, .such as the O pressure, in order to modulate the Mn/O ratio. As despicted in Supplementary Fig. 13d, when the average O/Mn ratio is approximately 5/3, the charge can be rebalanced, resulting in the dielectric antiphase boundaries through a specific deposition process. However, due to the small presence of K^+/Na^+ at the boundaries, the actual O/Mn ratio may slightly decreased.

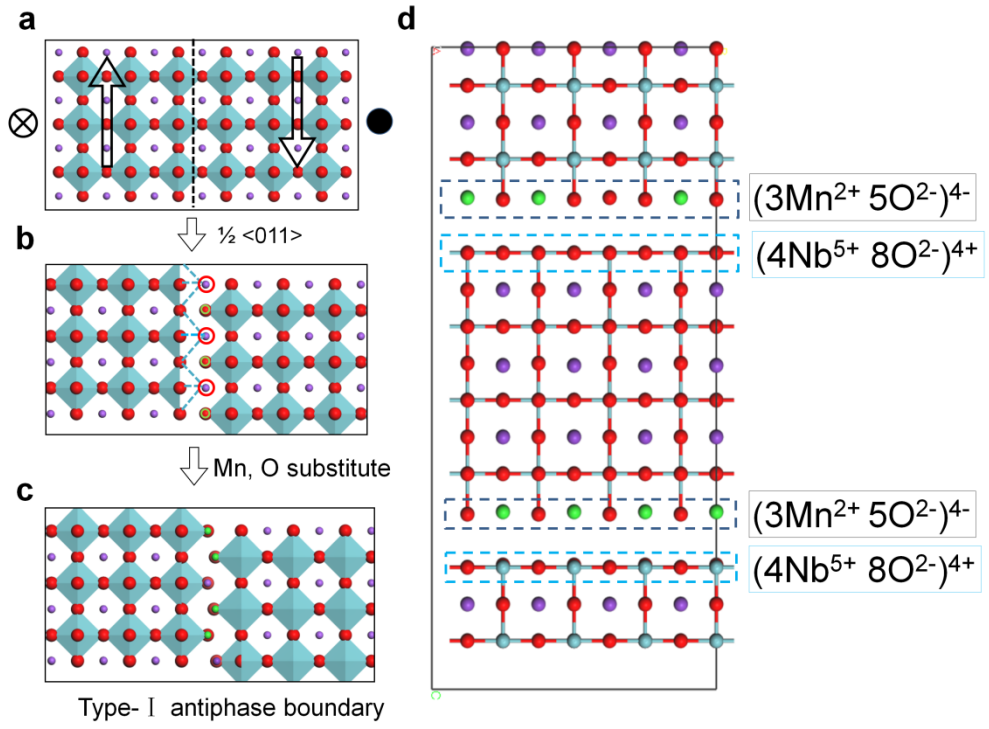

Supplementary Fig. 13| The schematic diagrams of charge balance for the Type-I antiphase boundaries. **a**, crystal structure model of classic perovskite KNN. **b**, crystal structure model of perovskite KNN lattice with relatively shift of 1/2 unit cell along the <011>, where the A-site and O vacuums are formed. **c**, crystal structure model of Type-I antiphase boundaries, in which the vacuums can be compensated with Mn and O. **d**, one possible local charge equilibrated atom structure for Type-I antiphase boundaries

Supplementary Fig. 14 illustrates the schematic diagram of charge balance of the Type-II antiphase boundaries. By shifting the perovskite lattice 1/2 unit cell along the <111> direction (as shown in Supplementary Fig. 14a), an additional O vacancy and one cation vacancy can be generated for each unit cell at the antiphase boundary, as depicted in Supplementary Fig. 14b. When an anion O^{2-} and cation Mn^{2+} occupy these vacancies, the charge remains in equilibrium (as shown in Supplementary Fig. 14c). At the Type-II antiphase boundaries, the cation atom columns and O atom columns are separated. In our experiment, we observed the presence of Nb/Mn/K/Na/O elements at these boundaries. Fig.S14d presents a possible local atomic structure for the Type-II antiphase boundaries, which includes Nb/Mn/K/Na/O atoms and allows for charge equilibration.

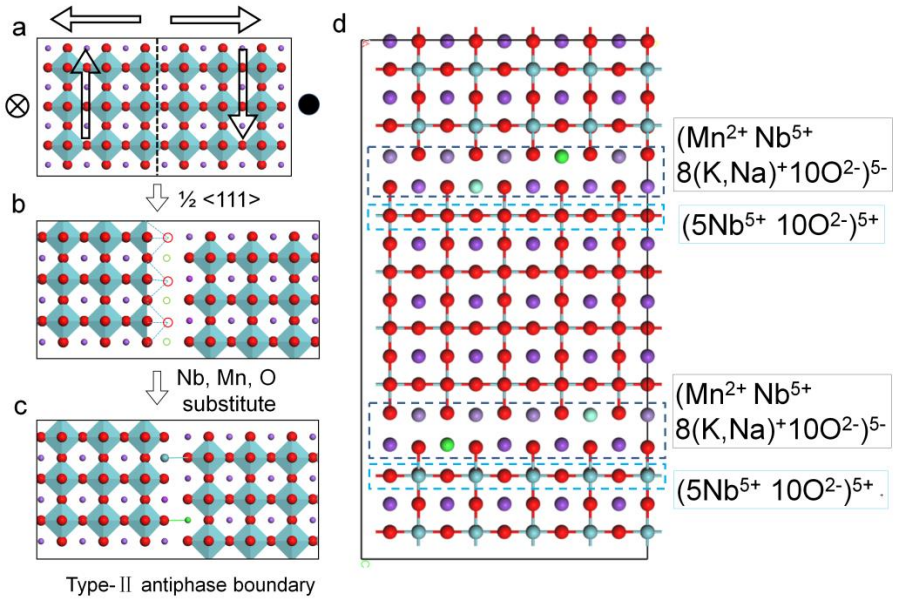

Supplementary Fig. 14| The schematic diagrams of charge balance for the Type-II antiphase boundaries. a, crystal structure model of classic perovskite KNN. **b**, crystal structure model of perovskite KNN lattice with relatively shift of 1/2 unit cell along the <111> direction. **c**, crystal structure model of Type-II antiphase boundaries. **d**, a possible local charge equilibrated atom structure for Type-II antiphase boundaries.

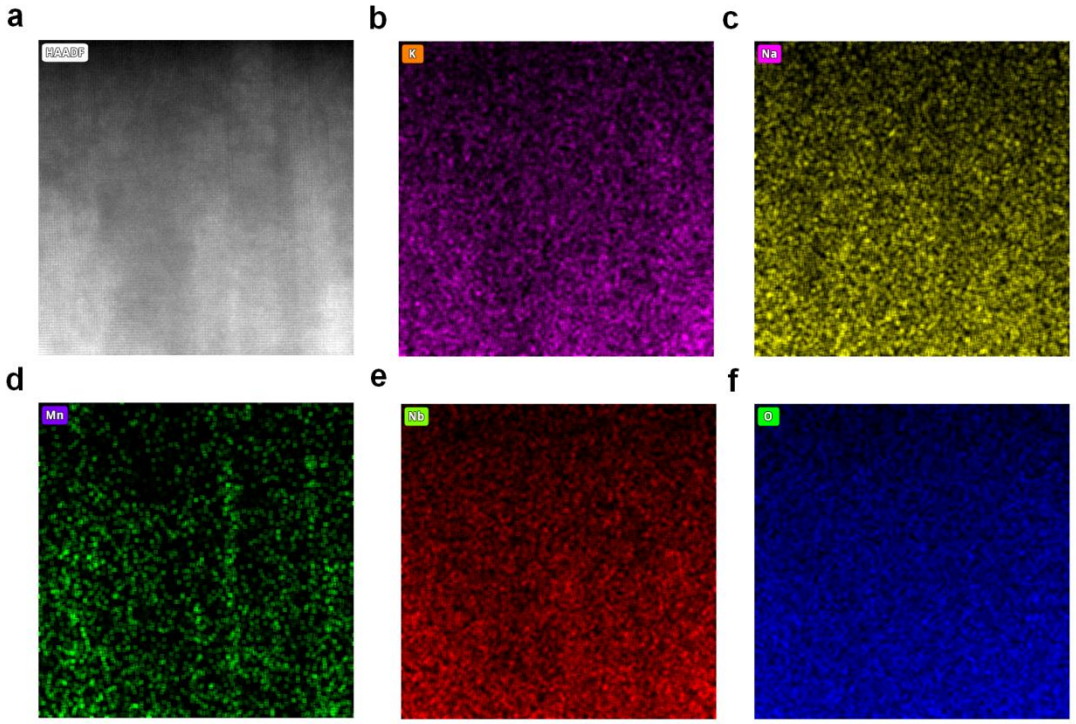

Supplementary Fig. 15| The microstructure and chemical composition of 1wt% Mn-doped KNN thin films. a, HAADF image in the out-of-plane direction. b-f, corresponding element mappings of K, Na, Mn, Nb, and O.

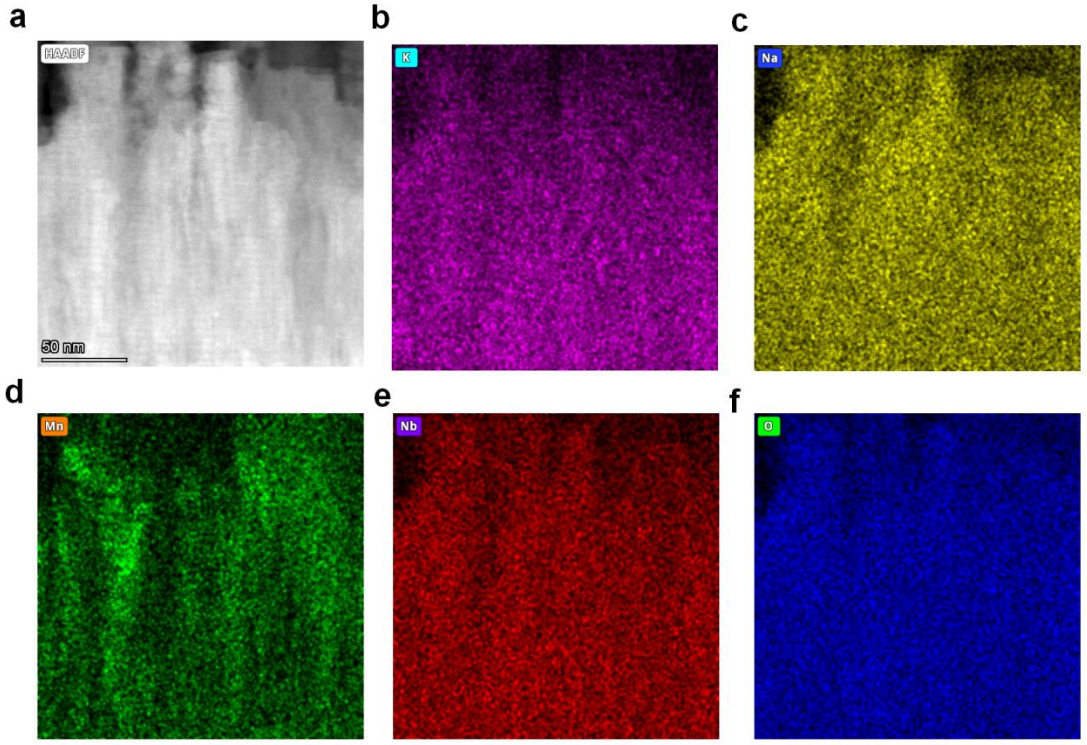

Supplementary Fig. 16| The microstructure and chemical composition of 5wt% Mn-doped KNN thin films. a, HAADF image in the out-of-plane direction. b-f, corresponding element mappings of K, Na, Mn, Nb, and O.

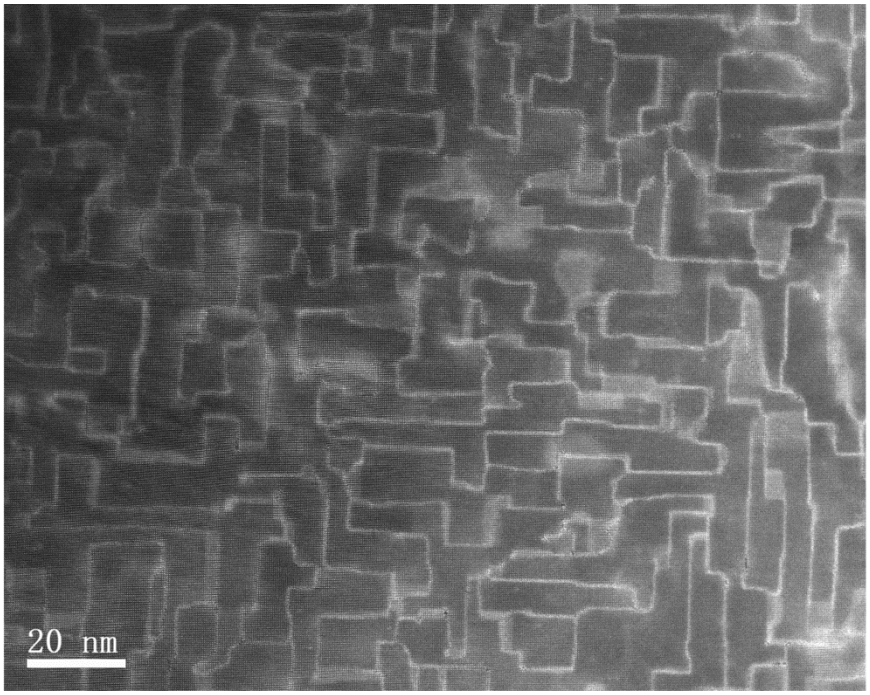

Supplementary Fig. 17| In-plane ADF image of KNN-M thin films, where the strain cause the extra bright image contrast at the boundaries.

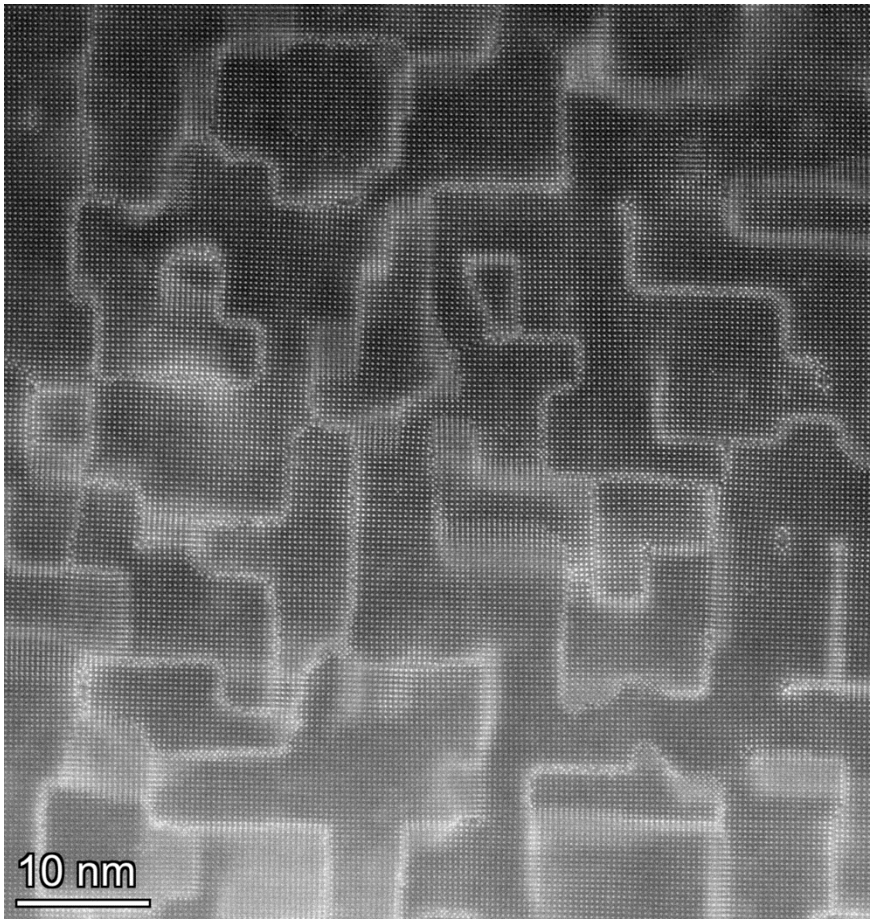

Supplementary Fig. 18| Atomic resolution ADF image of KNN-M thin films along the in-plane direction, where the strain cause the extra bright image contrast at the boundaries.

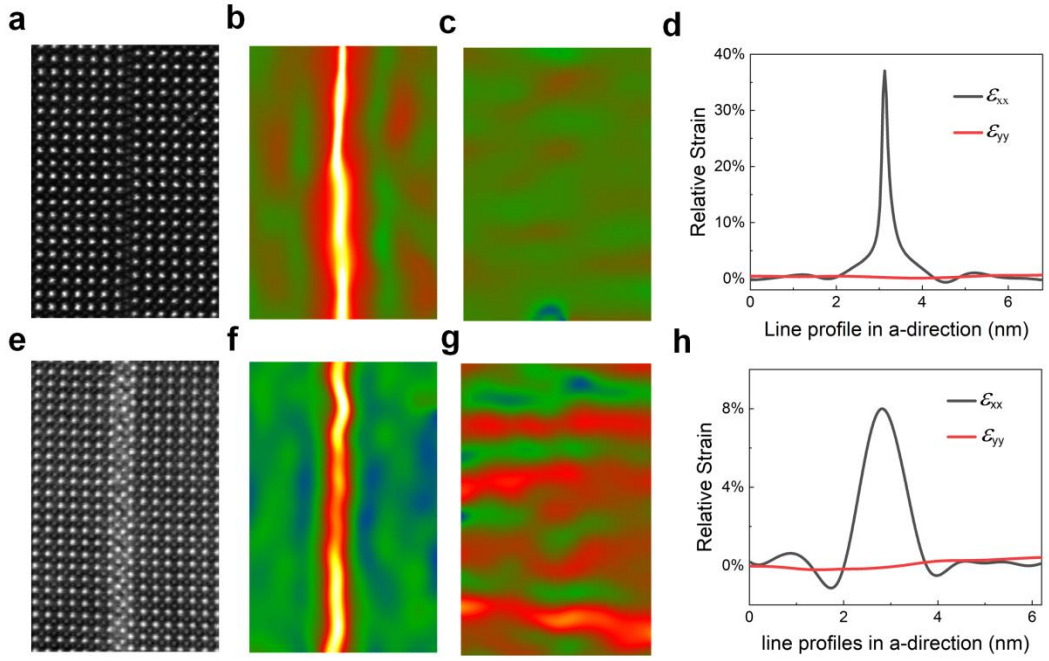

Supplementary Fig. 19| geometry phase analysis of Mn-inlaid antiphase boundaries. a, ADF image of I-type antiphase boundary, **b&c**, corresponding relative

lattice strain ε_{xx} and ε_{yy} mapping. **d**, the line profiles of ε_{xx} and ε_{yy}. **e,** ADF image of II-type antiphase boundary, **f&g**, corresponding relative lattice strain ε_{xx} and ε_{yy} mapping. **h**, the line profiles of ε_{xx} and ε_{yy}.

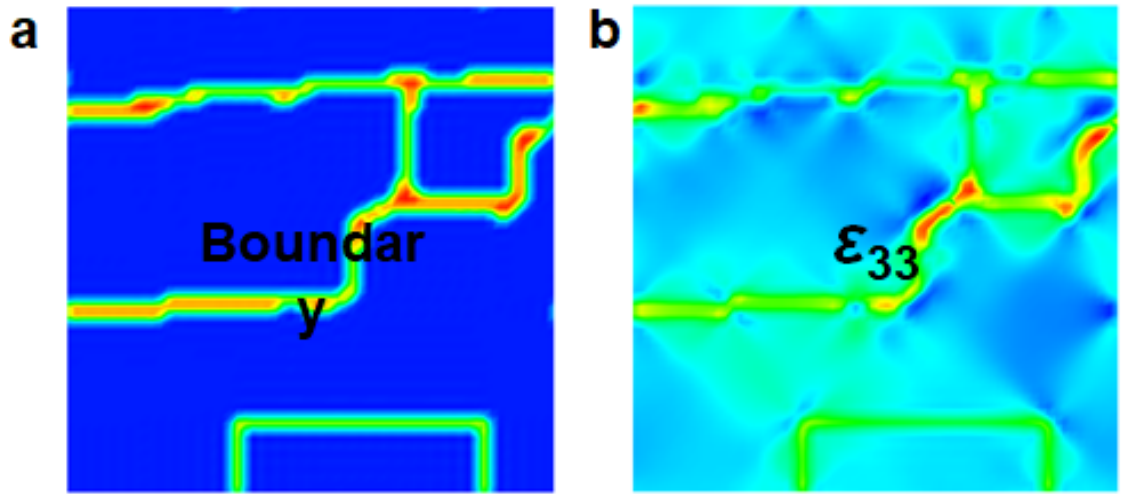

Supplementary Fig. 20| The boundary and strain condition used in simulations. $\varepsilon_{local}=\varepsilon_{33}$ have been used in our simulations to study the local strain's effect on microstructural evolution and *P-E* loop.

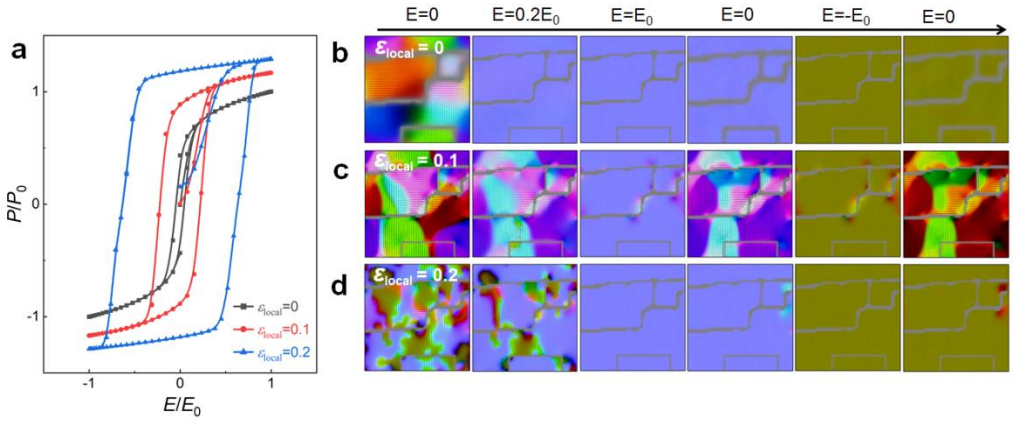

Supplementary Fig. 21| Calculated *P-E* loops and related micro structural evolution for KNN-M with different strains. a, Calculated *P-E* curves for KNN-M with different local strain value ε_{local}, we observed that the polarizations in the out-of-plane directions increased with the lattice strain increment during the application of the electric field, leading to a larger polarization in the ferroelectric loop. **b-d,** Related polarization evolution under one cycling for ε_{local} = 0, ε_{local} = 0.1, and ε_{local}=0.2. Different colors represent different polarization directions, light bule represent positive Tz, clay bank represents the negative Tz. As the applied external electric field increased, the polarizations changed from the O phase (shown in different colors) to the T phase (indicated by light blue or earthy yellow).

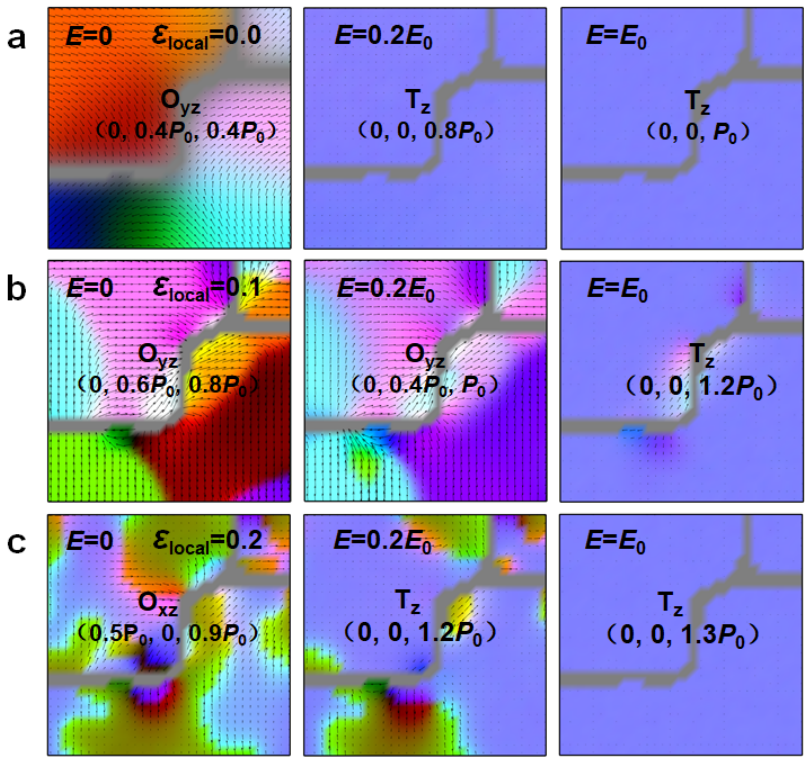

Supplementary Fig. 22| Enlarged microstructure evolution under different applied electric field from 0 to E_0 for different local strain. a ε_{local}=0, **b** ε_{local}=0.1, and **c** ε_{local}=0.2. Different colors represent different polarization directions, cyan represents positive O_{yz}, Orange represents positive O_{xz}, light bule represents positive T_z, claybank represents the negative T_z. The lattice strains around the boundaries induced larger polarization in both in-plane and out-of-plane directions.

34. P. A. van Aken, B. Liebscher, Quantification of ferrous/ferric ratios in minerals: new evaluation schemes of Fe L23electron energy-loss near-edge spectra. *Phys. Chem. Miner.* **29**, 188-200 (2002). doi: 10.1007/s00269-001-0222-6.

35. D. B. Loomer, T. A. Al, L. Weaver, S. Cogswell, Manganese valence imaging in Mn minerals at the nanoscale using STEM-EELS. *Am. Mineral.* **92**, 72-79 (2007). doi: 10.2138/am.2007.2252.